NEUROSCIENCE

Engineered glycomaterial implants orchestrate large-scale functional repair of brain tissue chronically after severe traumatic brain injury

Charles-Francois V. Latchoumane[1,2], Martha I. Betancur[3], Gregory A. Simchick[4,5], Min Kyoung Sun[1,6], Rameen Forghani[1], Christopher E. Lenear[1,2], Aws Ahmed[1,2], Ramya Mohankumar[1], Nivedha Balaji[1], Hannah D. Mason[1], Stephanie A. Archer-Hartmann[7], Parastoo Azadi[7], Philip V. Holmes[6,8], Qun Zhao[1,4,5], Ravi V. Bellamkonda[3], Lohitash Karumbaiah[1,2,6]*

Severe traumatic brain injury (sTBI) survivors experience permanent functional disabilities due to significant volume loss and the brain's poor capacity to regenerate. Chondroitin sulfate glycosaminoglycans (CS-GAGs) are key regulators of growth factor signaling and neural stem cell homeostasis in the brain. However, the efficacy of engineered CS (eCS) matrices in mediating structural and functional recovery chronically after sTBI has not been investigated. We report that neurotrophic factor functionalized acellular eCS matrices implanted into the rat M1 region acutely after sTBI significantly enhanced cellular repair and gross motor function recovery when compared to controls 20 weeks after sTBI. Animals subjected to M2 region injuries followed by eCS matrix implantations demonstrated the significant recovery of "reach-to-grasp" function. This was attributed to enhanced volumetric vascularization, activity-regulated cytoskeleton (Arc) protein expression, and perilesional sensorimotor connectivity. These findings indicate that eCS matrices implanted acutely after sTBI can support complex cellular, vascular, and neuronal circuit repair chronically after sTBI.

INTRODUCTION

Severe traumatic brain injuries (sTBIs) caused by blunt force or penetrating trauma to the brain lead to extensive tissue loss and lifelong disabilities (*1*). Although sTBIs account for only 10% of the approximately 1.7 million TBI cases reported in the United States annually, they are responsible for over 90% of all TBI-associated costs (*1*). There are no effective treatments to prevent cognitive impairments and tissue loss encountered after sTBI. Neural stem cells (NSCs) have long held a privileged position in neural repair strategies for their ability to mediate neuroprotective "bystander" signaling (*2*). However, inadequate control over NSC differentiation and the risk of immune rejection of xenografted NSCs pose serious limitations for their clinical application (*3*, *4*). Although autologous cell therapies could help mitigate some of these concerns (*5*), issues related to poor survivability of transplanted cells (*6*), and the risk of tumorigenesis in the case of human embryonic and pluripotent stem cells (*7*, *8*), pose significant barriers to clinical success.

Chondroitin sulfate proteoglycans (CSPGs) are major constituents of the brain extracellular matrix (ECM) and stem cell niche (*9*–*15*). CSPG-linked sulfated CS glycosaminoglycan (CS-GAG) side chains regulate growth factor signaling (*16*–*19*), neuronal development (*20*), and neuroplasticity (*21*, *22*). Fibroblast growth factor 2 (FGF2) and brain-derived neurotrophic factor (BDNF) bind with high affinity to sulfated CS chains via specific sulfation motifs that act as molecular recognition sites (*23*). FGF2 is expressed by NSCs and radial glial cells found in neurogenic niches of the brain (*24*), where it is known to promote neuroprotection (*25*), NSC migration and proliferation (*26*, *27*), and neurogenesis (*24*, *26*, *28*). BDNF is an important mediator of neuroplasticity at all stages of brain development (*29*) and is known to promote neuroprotection (*30*) and functional repair of the injured brain (*29*, *31*, *32*). FGF2 and BDNF also promote angiogenesis after injury (*16*, *33*–*35*) and are critical for the maintenance of oxygen perfusion and tissue viability after injury.

The development of acellular three-dimensional (3D) constructs that can potentiate cellular and functional brain repair has received much attention (*18*, *19*, *23*, *36*, *37*). A range of natural (*38*–*41*) and synthetic (*42*, *43*) polymer composites, as well as natural ECM-derived biomaterials (*44*, *45*) have been used for mediating brain tissue repair. When compared to these approaches, sulfated CS-GAGs have native functionality and sulfation motif–dependent high affinity to neurotrophic factors (*18*, *19*, *23*, *37*), making them ideal materials for mediating signal transduction of neurotrophic factors and complex endogenous tissue repair chronically after sTBI. In recent studies, acutely implanted 3D CS-GAG scaffolds with and without encapsulated NSCs enhanced the efficacy of endogenous NSCs and mediated neuroprotection 4 weeks after sTBI (*46*). However, the chronic functional implications of acellular, neurotrophic factor functionalized engineered CS (eCS) matrix implants after sTBI have so far not been assessed. eCS matrix implants that are designed to match the composition and biophysical properties of native brain ECM present an attractive approach for the treatment of sTBI-induced tissue and functional loss.

In this study, we conducted a systematic assessment of the long-term outcomes of implanting FGF2 and BDNF-laden sulfated eCS

[1]Regenerative Bioscience Center, University of Georgia, Athens, GA 30602, USA. [2]Edgar L. Rhodes Center for ADS, College of Agriculture and Environmental Sciences, University of Georgia, Athens, GA 30602, USA. [3]Department of Biomedical Engineering, Pratt School of Engineering, Duke University, 101 Science Drive, Durham, NC 27705, USA. [4]Department of Physics and Astronomy, University of Georgia, Athens, GA 30602, USA. [5]Bio-Imaging Research Center, University of Georgia, Athens, GA 30602, USA. [6]Division of Neuroscience, Biomedical & Health Sciences Institute, University of Georgia, Athens, GA 30602, USA. [7]Complex Carbohydrate Research Center, University of Georgia, Athens, GA 30602, USA. [8]Psychology Department, University of Georgia, Athens, GA 30602, USA.
*Corresponding author. Email: lohitash@uga.edu

matrices in rats subjected to sTBI. We performed magnetic resonance imaging (MRI) phase gradient analyses of regional cerebral blood flow (rCBF) and tissue vascularization in conjunction with longitudinal behavioral performance and functional recovery, followed by detailed terminal immunohistochemical assessments of tissue-specific biomarkers. We also quantified activity-related cytoskeletal associated protein (Arc) expression and volumetric vasculature tracing in cleared brain tissue to localize newly formed functional clusters of neurons intra- and perilesionally in sTBI rats implanted with eCS scaffolds when compared to controls.

RESULTS

Acutely implanted eCS matrices promote chronic neuroprotection and recovery of gross motor function

To assess the chronic neuroprotective effects of neurotrophic factor–laden eCS matrix implants (fig. S1), we performed controlled cortical impact (CCI)–induced sTBI in the caudal forelimb area (CFA) in rats and implanted eCS matrices 48 hours after CCI in the lesion epicenter. We performed longitudinal assessments of motor function and MRI-based quantification of tissue volume loss and conducted terminal histological quantification of injury volume (Fig. 1A).

While general locomotion was found to be similar across all groups (fig. S2A), we observed that the performance of eCS matrix–implanted rats was found to be comparable to Sham controls, whereas sTBI rats demonstrated significant motor deficits (Fig. 1B and fig. S2B).

From results of longitudinal T_2-weighted MRI at 4- and 20-week time points and lesion volume analyses (Fig. 1, C and D), as well as terminal Nissl staining of tissue and quantification at 20 weeks after sTBI (Fig. 1, E and F), we were able to detect the significantly greater tissue atrophy in the sTBI-only animals when compared to eCS matrix–implanted rats and Sham controls (Fig. 1, D and F).

These results demonstrated that eCS matrix–implanted rats exhibited tissue and motor function recovery that was comparable to Sham control group animals chronically after sTBI.

eCS matrices mediate enhanced proliferation of endogenous NSCs and neurotrophic factor expression

CS matrices have been demonstrated to promote FGF2-mediated neural progenitor homeostasis and neuroprotection 4 weeks after sTBI (*17*, *46*). Considering these previous observations, we quantified the effects of neurotrophic factor–laden eCS matrices on the chronic maintenance of proliferating NSCs in the lesion site using Ki67 and Sox-1 biomarkers (Fig. 2, A and C) and CS-mediated FGF2 retention (Fig. 2, B, D, and E). Endogenous NSC proliferation in brain tissue from eCS matrix–implanted rats was found to be comparable to Sham controls (Fig. 2C and fig. S3, A, C, and D) but was significantly decreased in sTBI-only rats. Although a significant decrease in $Ki67^+$ cells in tissue from eCS-treated animals was observed when compared to Sham and TBI controls (fig. S3, A, B, and E), the significantly increased percentage of $Sox\text{-}1^+$ $Ki67^+$ cells in eCS matrix–treated animals when compared to TBI controls (Fig. 2C) suggests that NSCs do not contribute to the observed overall decrease in $Ki67^+$ cells. These findings were further corroborated by FGF2 expression levels (Fig. 2D), which followed a similar trend to $Sox\text{-}1^+$ staining. CS56 antibody staining of implanted eCS matrices and endogenously produced CS-GAGs in the lesion site revealed no significant differences in CS56 staining between TBI and eCS groups but indicated a significantly greater $CS56^+$ staining in both groups when compared to Sham control (Fig. 2E). Qualitative differences in locational presence of $CS56^+$ staining were observed throughout the lesion sites in eCS and sTBI-only animals. When compared to sTBI-only animals, which predominantly demonstrated $CS56^+$ staining only in the lesion penumbra and indicated a complete lack of cellular presence in the lesion volume, eCS matrix–treated animals indicated a uniform presence of $CS56^+$ staining throughout the lesion volume. The $CS56^+$ staining of eCS matrix–implanted brain tissue indicates the potential residual presence of eCS matrix along with what appears to be endogenously produced CS-GAGs/CSPGs 20 weeks after sTBI. These results suggest that eCS matrix implants might enhance NSC proliferation by facilitating the sustained expression and presence of FGF2 in the lesion site 20 weeks after sTBI.

We used laser capture microdissection (LCM) to isolate perilesional tissue labeled by rat immunoglobulin G (IgG) staining (Fig. 2F), along with any tissue present in the lesion cavity to specifically identify regional changes in expression of *BDNF*, *FGF2*, *CXCL12*, and *CXCR4* transcripts (Fig. 2G). We identified the significant and tissue-specific increase in expression levels of transcripts encoding neuroplasticity (*BDNF)* and neural progenitor proliferation (*FGF2)* factors, along with NSC homing (*CXCL12* and *CXCR4*) transcripts in brain tissue explanted from eCS matrix–treated animals when compared to Sham and TBI controls (Fig. 2G; >2-fold, $P < 0.05$). Fold differences in target gene expression in eCS matrix–implanted animals were compared to that of TBI rats after normalizing to Sham group expression levels and endogenous controls (*GADPH* and *HPRT1*).

eCS matrices promote chronic neurogenesis and neuroplasticity

Because cell proliferation, neuronal differentiation, and synaptic plasticity are indicators of normal brain tissue homeostasis (*47*, *48*), we considered the occurrence of these processes within the lesion site as measures of functional neuronal network activity, tissue maintenance, and recovery. We quantified the presence of newly formed neurons using markers for immature/migrating neuroblasts [doublecortin-positive (DCX^+)] and dividing [5-bromo-2′-deoxyuridine–positive ($BrdU^+$)] neuronal cells (Fig. 3, A and B). We found a significantly increased number of dividing cells in the eCS-implanted rats when compared to Sham and TBI groups (fig. S4, A to D). A similar trend was found for DCX^+ cells (fig. S4E) and $DCX^+/BrdU^+/DAPI^+$ (4′,6-diamidino-2-phenylindole–positive) colabeled cells in eCS-treated animals (Fig. 3B), demonstrating a significant increase in these markers when compared to Sham and TBI groups. These results indicate that eCS matrix implants might promote the differentiation of proliferating cells into new neurons at the lesion site up to 20 weeks after sTBI.

Because synaptic vesicle presence is indicative of functional neurons and synaptic plasticity (*49*), we evaluated the potential change in synaptic plasticity at the 20-week time point using antibodies against the synaptic vesicle marker synaptophysin I (Syn; Fig. 3C). We observed a significant increase in $Syn1^+$ signal in both $DAPI^+$ ($P = 0.014$; fig. S5, A to D) and $NeuN^+$ cells (Fig. 3D) in eCS matrix–implanted animals when compared to Sham and TBI-only rats.

Despite a net reduction in $Olig2^+$ cells in eCS-implanted animals (fig. S6, C and D), we observed a significantly higher percentage of

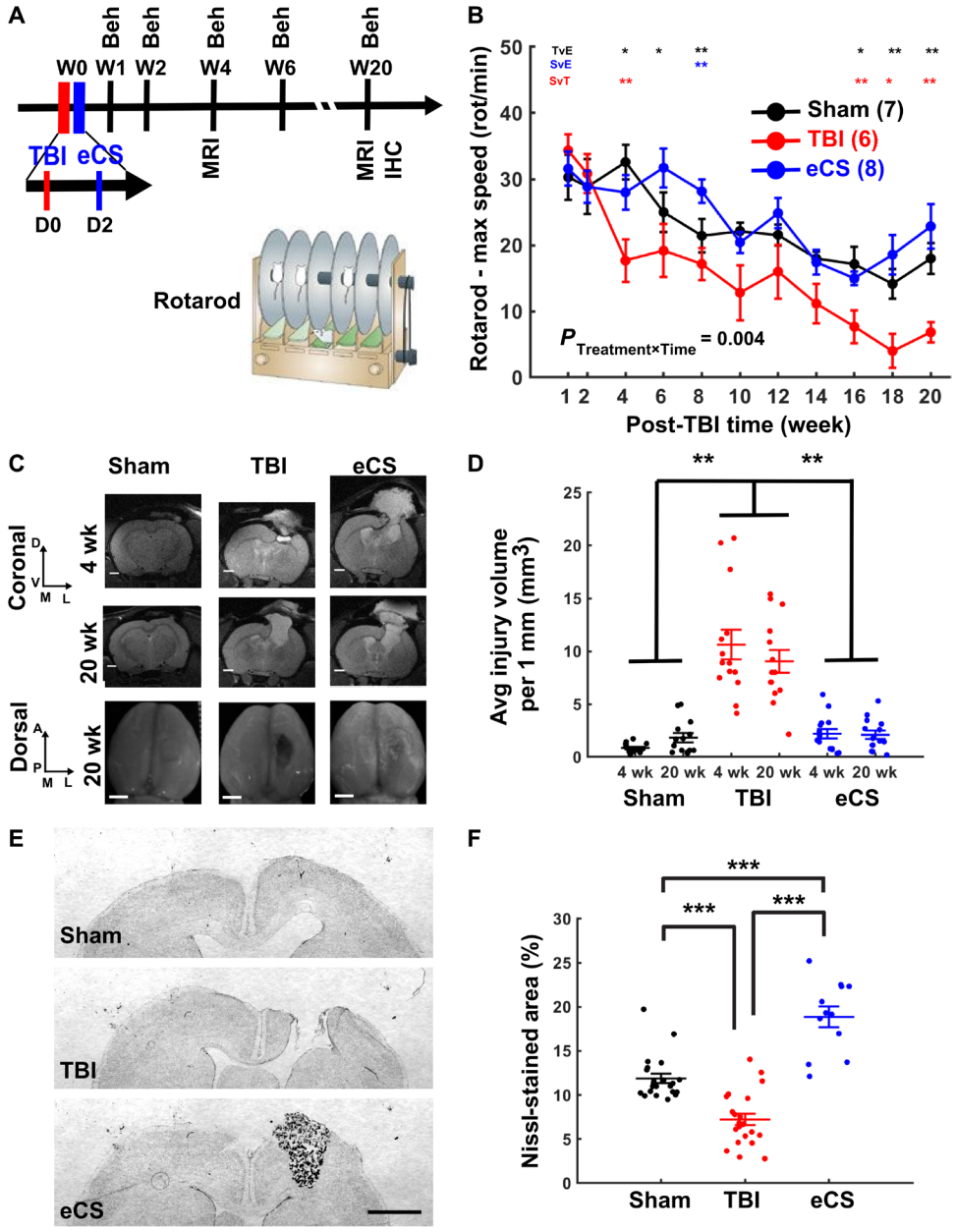

Fig. 1. eCS implants reduce lesion volume and improve gross motor function 20 weeks after sTBI. (**A**) Experimental schedule. All rats received an sTBI at week 0 (D0). eCS implants were intracortically administered 48 hours after sTBI (D2). Following 1 week of recovery, all rats underwent behavioral testing at weeks 1 and 2, and every other week thereafter (4, 6, 8, 10, 12, 14, 16, 18, and 20). (**B**) The rotarod test was used as a measure of balance and motor coordination. Two-way repeated-measures analysis of variance (ANOVA): $P_{Treatment} = 0.153$; $P_{Time} < 0.001$; $P_{TreatmentxTime} = 0.004$. Post hoc multiple comparisons using Dunn-Sidak correction are shown above each time point for Sham versus TBI (red), Sham versus eCS (blue), and TBI versus eCS (black). (**C**) Representative T_2-weighted (T2W) MRI images (top) for each treatment group Sham, TBI, and eCS (coronal section); scale bars, 500 μm; top view of the extracted brain (bottom); scale bars, 1 mm. D, dorsal; V, ventral; M, middle; L, lateral; A, anterior; P, posterior. (**D**) Average injury volume was quantified for each 1-mm slice around the injury and based on the T2W MRI images (mm^3). Two-way repeated-measures ANOVA; treatment factor: $P < 0.001$; time factor: $P = 0.53$; treatment × time: $P = 0.0279$. (**E**) Representative Nissl-stained coronal sections of rat brain for the Sham, TBI, and eCS groups. Scale bar, 1 mm. (**F**) Lesion volume quantification using Nissl stain for Sham (six rats, four images per rat), TBI (six rats, four images per rat), and eCS (three rats, four images per rat) groups. One-way ANOVA; treatment: $P < 0.001$. Post hoc least significant difference (LSD), $^*P < 0.05$, $^{**}P < 0.01$, and $^{***}P < 0.001$. Graphs show means ± SEM.

$Olig2^+$ cells colocalized with $NeuN^+$ cells in eCS rats when compared to those in the Sham and TBI groups (fig. S6, A to C and E). In contrast to these findings, the colocalization of $NeuN^+$ and $Olig2^+$ relative to $DAPI^+$ was found to be significantly reduced in TBI rats (fig. S6, B and F) when compared to Sham and eCS matrix–implanted animals.

Together, these results suggest that despite a significant reduction in the number of neurons following sTBI, eCS matrix implants

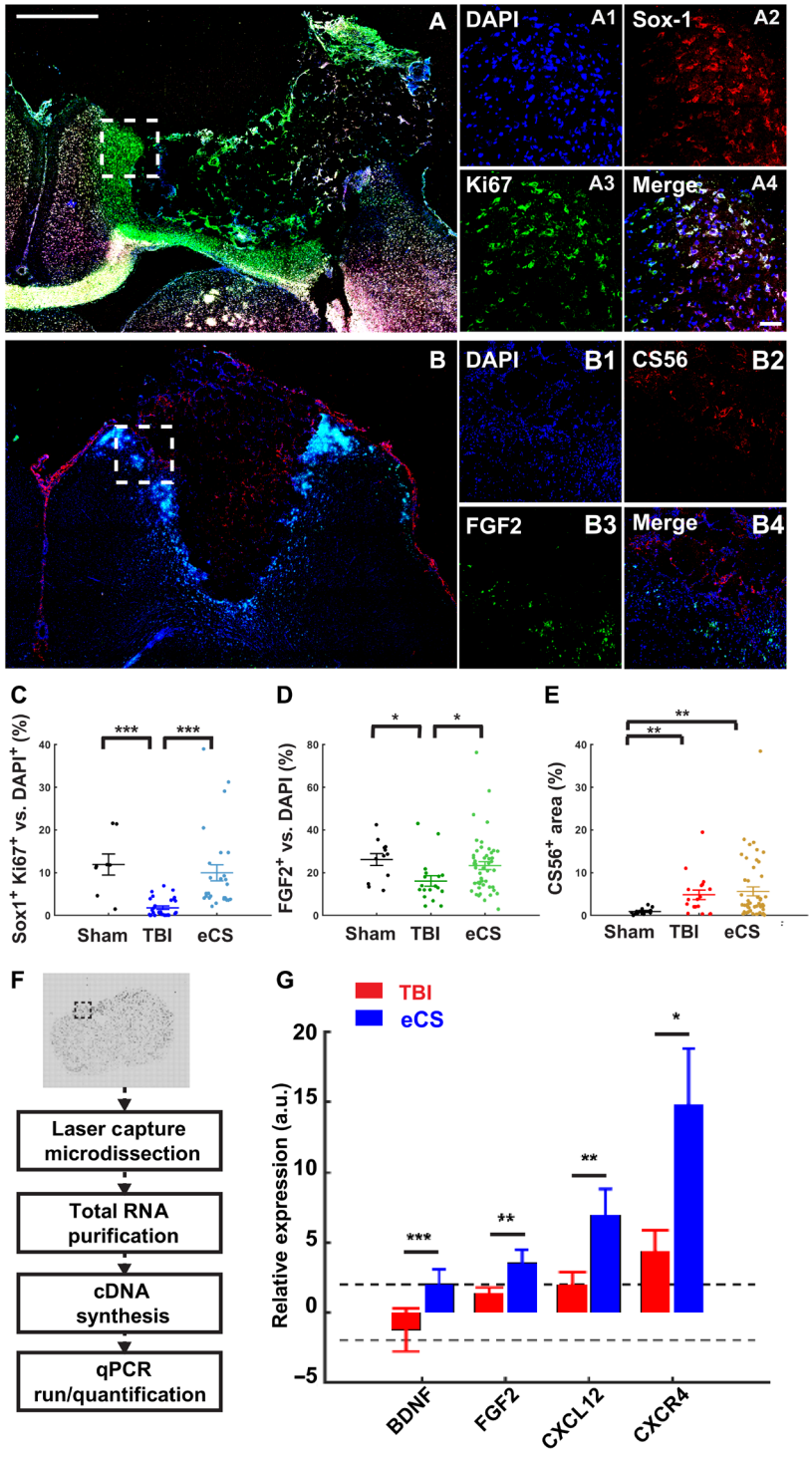

Fig. 2. eCS implants promote NSC proliferation and neurotrophic factor expression 20 weeks after sTBI. (**A**) Representative tiled images of ipsilesional hemisphere (left coronal sections) of eCS rat brain tissue; scale bar, 1 mm. (A1 to A4) Representative magnification of dashed white square shown in (C) for DAPI (A1), Sox-1 (A2), Ki67(A3), and merged (A4); scale bar, 100 μm. (**B**) Representative tiled images of ipsilesional hemisphere (left coronal sections) of eCS rat brain tissue; scale bar, 1 mm. (B1 to B4) Representative magnification of dashed white square shown in (A) for DAPI (B1), CS56 (B2), FGF2 (B3), and merged (B4); scale bar, 100 μm. (**C**) Colocalization of Sox-1$^+$ cells with Ki67$^+$ cells as a percentage of Ki67$^+$ cells for each treatment. Kruskal-Wallis, treatment: $P < 0.001$. (**D**) Colocalization of FGF2$^+$ cells with DAPI$^+$ cells as a percentage of DAPI$^+$ cells for each treatment. Kruskal-Wallis, treatment: $P < 0.05$. (**E**) CS56$^+$ percentage area for each treatment. Kruskal-Wallis, treatment: $P < 0.001$. Post hoc LSD Mann-Whitney *U* test, *$P < 0.05$, **$P < 0.01$, and ***$P < 0.001$. (**F**) At 20-week time point, brains were flash-frozen and tissue was laser capture microdissected. Total RNA was purified and used to synthesize cDNA. Quantitative reverse transcription polymerase chain reaction (qRT-PCR) was performed using prevalidated primers of interest for quantification of gene expression. (**G**) Relative expression of *BDNF*, *FGF2*, *CXCL12*, and *CXCR4* transcripts in TBI and eCS treatment groups. Two-tailed *t* test, *$P < 0.05$, **$P < 0.01$, and ***$P < 0.001$. Graphs show means ± SEM.

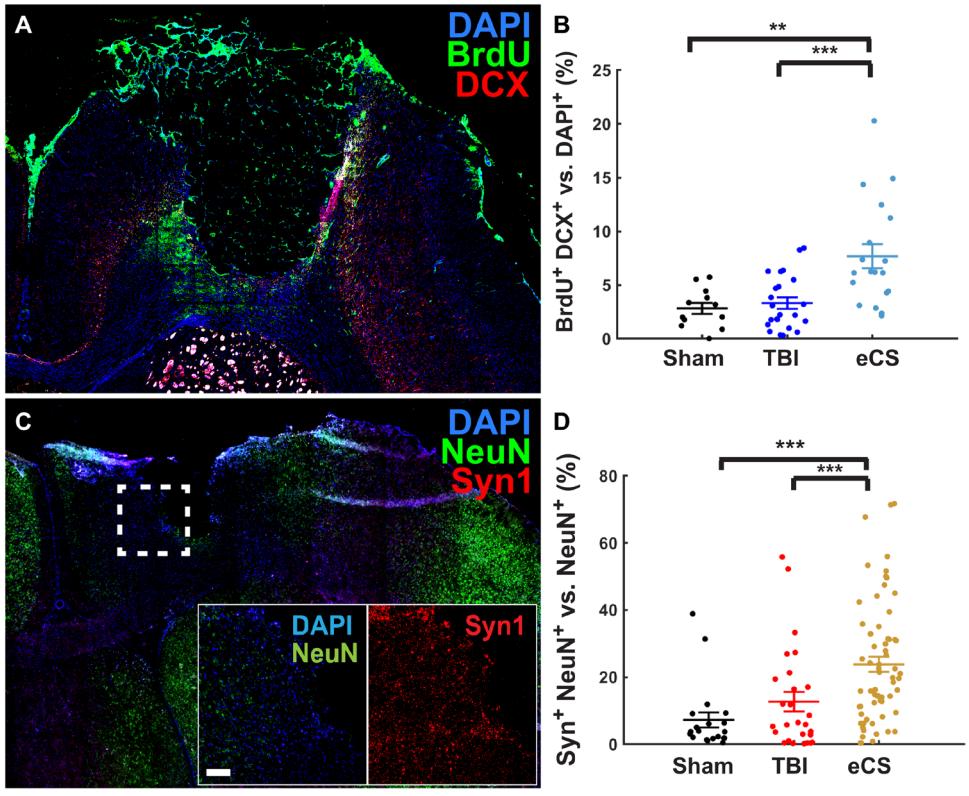

Fig. 3. eCS implants promote neurogenesis and plasticity 20 weeks after sTBI. (**A**) Representative tiled images of ipsilesional hemisphere (left coronal sections) coronal sections with merged DAPI (blue), DCX (red), and BrdU (green) staining of eCS rat brain tissue; scale bar, 1 mm. (**B**) Colocalization of DCX^+ and $BrdU^+$ cells with $DAPI^+$ cells as a percentage of $DAPI^+$ cells for each treatment; Kruskal-Wallis, treatment: $P < 0.001$. (**C**) Representative tiled images of ipsilesional hemisphere (left coronal sections) with merged DAPI (blue), Syn1 (red), and NeuN (green) staining of eCS rat brain tissue; scale bar, 1 mm. Inset shows magnified images of $DAPI^+$ and $NeuN^+$ cells (merged; left) and $Syn1^+$ cells (right) from the region represented by the dashed white square; scale bar, 100 μm. (**D**) Colocalization of Syn^+ cells with $NeuN^+$ cells as percentage of $NeuN^+$ cells for each treatment. Kruskal-Wallis, treatment: $P < 0.001$. Post hoc LSD Mann-Whitney *U* test, $^*P < 0.05$, $^{**}P < 0.01$, and $^{***}P < 0.001$. Graphs show means ± SEM.

promoted cell proliferation, neuronal differentiation, synaptic plasticity, and potential myelination of newly formed neurons present intra- and perilesionally.

eCS matrix implants attenuate the chronic presence of neuroinflammatory cells

Attenuated influx of neuroinflammatory cells chronically after sTBI could prevent prolonged tissue damage and atrophy and is a marker of a favorable tissue response after TBI (*50*). To mark the chronic presence of activated macrophages and reactive astrocytes that are characteristic of a neuroinflammatory cellular response to brain injury, we quantified $CD68^+$-activated macrophages and glial fibrillary acidic protein–labeled ($GFAP^+$) reactive astrocytes (fig. S7, A to C). We observed that eCS matrix–implanted rats had similar levels of $CD68^+$ cells (fig. S7D) as Sham controls, while TBI rats showed a significant decrease in $CD68^+$ cells compared to Sham and eCS matrix–implanted rats. While Sham and eCS rats showed similar $GFAP^+$ expression levels, TBI rats in comparison demonstrated a significant increase in $GFAP^+$ area (fig. S7E). Although the TBI animals demonstrated a significant reduction in activated macrophage response, we speculate that this is likely due to the significant tissue loss and absence of intralesional tissue in TBI animals when compared to Sham controls and eCS-treated animals. Overall, these results suggest the prevalence of an attenuated neuroinflammatory cellular response in eCS animals 20 weeks after sTBI.

eCS matrices enhance local vascularization and global blood flow

Because inadequate vascularization is often responsible for the failure of implanted biomaterials (*51*), we investigated the extent of tissue neovascularization in eCS matrix–implanted animals when compared to controls, using collagen IV ($Col\text{-}IV^+$) and rat endothelial cell antigen ($Reca1^+$) markers (Fig. 4, A and B). We also used MRI phase gradient imaging of CBF as a measure of vascular function (Fig. 4, C to F).

We found a significant increase in $Reca1^+$ (fig. S8D) and $Col\text{-}IV^+$ (fig. S8E) expression percentage area in the eCS matrix–treated animals compared to both Sham and TBI controls. Notably, Reca1 and Col-IV colocalization was detected to be ~60% in Sham and eCS matrix–treated groups, which was significantly enhanced when compared to the TBI group (Fig. 4B).

Because a significant reduction of CBF chronically is linked to cognitive dysfunction and poor prognosis in humans with sTBI (*52*–*56*) and is also associated with the lack of neuronal activity and loss of neuronal volume in humans and rats (*57*, *58*), we assessed CBF using MRI-based normalized phase gradient (nPG) mapping

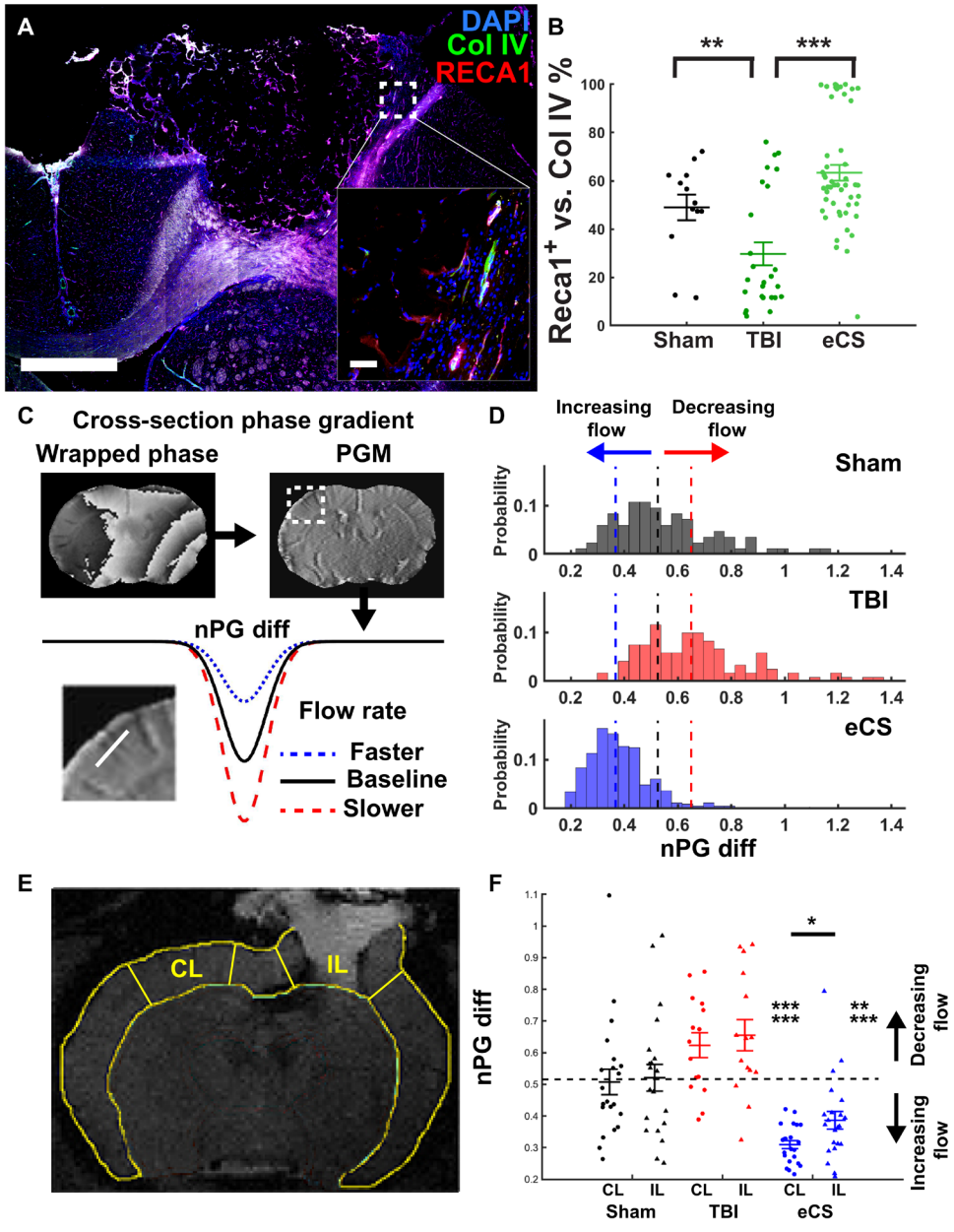

Fig. 4. eCS matrices promote vascularization and increased CBF 20 weeks after sTBI. (**A**) Representative tiled image of ipsilesional hemisphere of the eCS group; scale bar, 1 mm. (**B**) Colocalization of Reca1$^+$ cells with Col IV$^+$ cells as a percentage of Col IV$^+$ cells for each treatment. Kruskal-Wallis, treatment: $P < 0.001$. Post hoc LSD Mann-Whitney *U* test, $^*P < 0.05$, $^{**}P < 0.01$, and $^{***}P < 0.001$. (**C**) Phase gradient was estimated from MRI. First, the wrapped phase map (top left) was used to generate phase gradient maps (PGMs; top right) for each slice by calculating the magnitude of the phase gradients determined in the readout and phase encoding directions (see Materials and Methods for details). Bottom: nPG differences between a vessel and the surrounding tissue were measured across all distinguishable vessels at the coronal cross section (inset, white line). Note: The rate of flow in a blood vessel is inversely proportional to the change in phase between the vessel and the surrounding tissue (see Materials and Methods). (**D**) Distribution of nPG for all identified blood vessels in Sham ($n = 84$), TBI ($n = 121$), and eCS ($n = 432$) groups. Dashed line represents the median nPG for Sham (black), TBI (red), and eCS (blue). One-way ANOVA, $F(2) = 230.56$, $P = 8.57 \times 10^{-51}$/measure effect size $P < 0.001$. (**E**) Representative segmentation of MRI coronal brain slice for regional and hemispheric comparison of blood flow. IL, ipsilesional; CL, contralesional. (**F**) nPG for the perilesional region of interest (ROI) and matching ROI in the contralateral hemisphere. Two-way ANOVA, treatment: $P < 0.0001$. Post hoc one-sample *t* test; post hoc LSD, $^*P < 0.05$, $^{**}P < 0.01$, and $^{***}P < 0.001$. Graph shows means ± SEM.

of identified blood vessels in the lesion (Fig. 4C). We observed a significantly enhanced overall CBF in eCS matrix–implanted rats (Fig. 4D and fig. S9; estimation statistics) when compared to Sham animals, while TBI control animals showed a statistically insignificant decrease in measured CBF. Using ipsi- and contralesional region of interest (ROI) measurements (Fig. 4E), we detected a specific increase in cortical CBF in eCS matrix–implanted rats with a significantly higher CBF detected in the contra- versus ipsilesional side (Fig. 4F). Together, these results indicate that eCS matrix–implanted rats demonstrate chronically enhanced neovascularization

perilesionally, along with significantly enhanced CBF both contra- and ipsilesionally when compared to TBI-only controls.

eCS matrices promote chronic forelimb-specific functional recovery and activation of activity-regulated cytoskeleton-associated protein (Arc) in RFA

We used a skilled reach task (SRT) to investigate the circuit-specific implications of the neuroprotective, neurogenic, and angiogenic attributes of eCS matrix implants following sTBI. The SRT was used as a forelimb-specific assessment of motor recovery followed immediately by terminal volumetric imaging of activity-regulated cytoskeleton-associated protein (Arc^+). This made it possible to assess task-specific responses following a lesion of the M2–reach-to-grasp region in the rostral forelimb area (RFA).

We found that eCS matrix–implanted rats that trained for 2 weeks on the SRT (Fig. 5A) demonstrated reach-to-grasp performance recovery from week 2 that was comparable to Sham animals and that persisted up to week 8 (Fig. 5B and fig. S10). TBI control rats showed significant forelimb functional deficits throughout the 8 weeks of testing, with a transient improvement that lasted about 3 weeks (weeks 4 to 6) before significantly worsening at week 8. The quantification of ipsi- and contralesional Arc^+ neurons (Arc^+/$NeuN^+$ coexpression; Fig. 5C) immediately after reach-to-grasp activity showed strong activation within anterior and posterior RFA regions and low contralateral signal in Sham animals (Fig. 5D). TBI control rats, in comparison, showed little to no ipsilesional RFA activity with notable contralesional activation when compared to eCS matrix–implanted rats, which demonstrated Arc^+ signal within the RFA lesion in addition to contralesional activation.

Perilesional laminar recordings of multiunit activity reveal the preservation of sensorimotor responses 10 weeks after sTBI in eCS matrix–implanted rats

We stimulated the contralesional paw using low-intensity electrical pulses to further investigate whether eCS matrix implants directly facilitated recovery of sensorimotor responses (fig. S11A). We

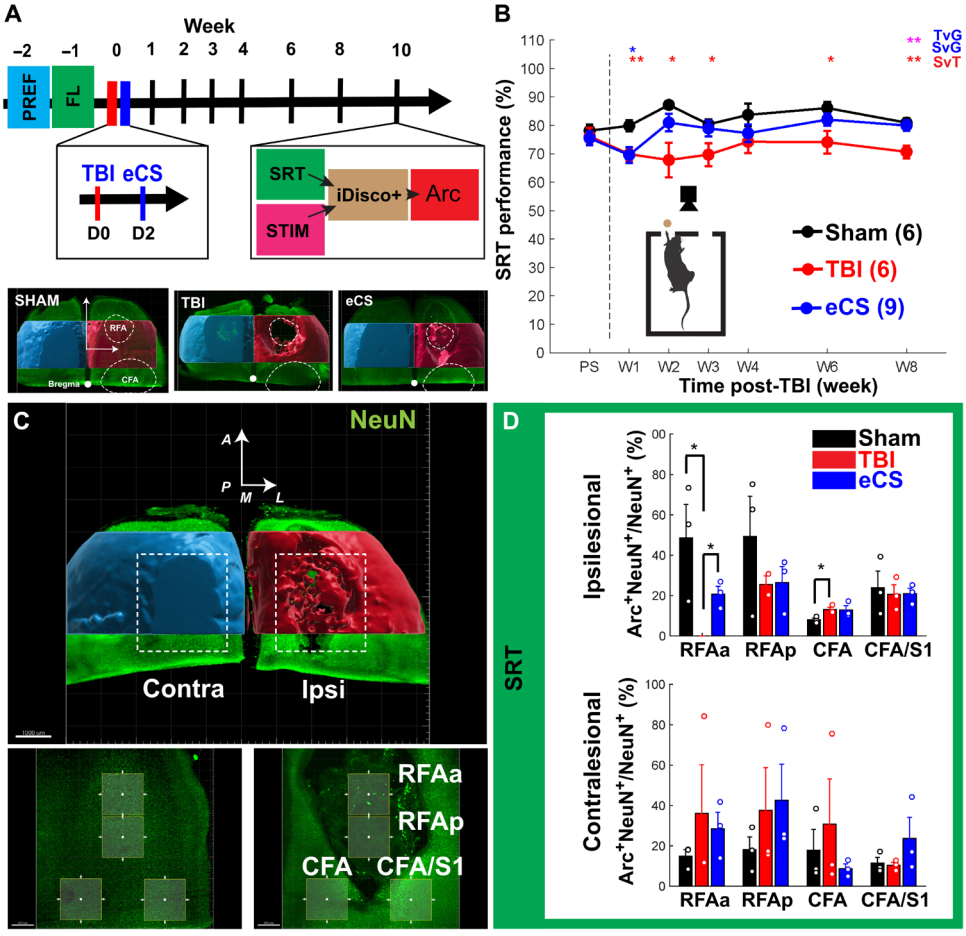

Fig. 5. eCS matrix–implanted animals demonstrate enhanced recovery of reach-to-grasp–specific motor function 8 to 10 weeks after sTBI. (**A**) Experimental schedule of SRT preference (PREF) and forced left (FL) limb training before TBI induction and eCS matrix implantation (top). Volumetric mapping of lesion from $iDisco^+$ cleared and $NeuN^+$ stained Sham-treated (left), TBI-treated (middle), and eCS-treated (right) brains (bottom). Contra- and ipsilesional hemispheres are colored blue and red, respectively. (**B**) Overall SRT performance of Sham ($n = 6$), TBI ($n = 6$), and eCS ($n = 9$) groups after sTBI and treatment. Repeated-measures ANOVA, time: $P < 0.05$, group: $P < 0.01$, time × group: $P = 0.1306$; post hoc LSD, $^*P < 0.05$ and $^{**}P < 0.01$. Color-coded group comparisons indicate Sham versus TBI (SvT; red), Sham versus eCS (SvG; blue), and TBI versus eCS (TvG; magenta). RFAa, RFA anterior; RFAp, RFA posterior. (**C**) ROI analysis of Arc^+ $NeuN^+$ colocalization and reach-to-grasp function mapping. The ipsi- and contralesional sides are marked in red and blue, respectively. (**D**) Ipsilesional (top) and contralesional (bottom) quantification of Arc^+ $NeuN^+$ colocalized cells after SRT assay. Sham ($n = 3$), TBI ($n = 3$), and eCS ($n = 3$). Line plots and bar graphs show means ± SEM. $^*P < 0.05$.

evaluated the spontaneous and evoked (fig. S11, B and C) electrophysiological responses from the intact M1 and M1/S1 regions using a 32-channel laminar electrode (fig. S11D). We observed that following sTBI, a rapid response to electrical stimulation of the left paw reduced in occurrence rate and increased in time jittering in all cortical layers and in the two recording positions CFA and CFA/S1 (fig. S11E). Notably, the late response recorded in the CFA region in response to paw stimulation showed an increased delay in TBI animals (fig. S11E, left; mean jitter: 36.5 ms), which was found to be faster in eCS matrix–implanted rats (mean jitter: 15.1 ms). This effect was not detected in CFA/S1 region (fig. S11E, right). The TBI control rats also showed a sustained post-stimulation activity registered during nonstimulation recording periods when compared to the prestimulation epochs (fig. S12), which was not observed in Sham and eCS matrix–implanted rats. We also found that paw stimulation induced differential activation of the CFA/S1 and CFA motor area, with TBI control animals demonstrating a marked reduction and eCS matrix-implanted animals showing a marked increase in activation respectively. These results indicate that the response and activation of the perilesional circuitry associated with sensorimotor function of forelimb were reduced in TBI rats and partially recovered in eCS matrix–implanted rats.

RFA-specific revascularization explains neuronal presence and behavioral performance

We performed brain tissue clearing to specifically investigate whether vascular architecture could reveal a stronger correspondence between vasculature features (Fig. 6), neuronal presence, and behavioral performance.

Following Imaris-based vasculature tracing (Fig. 6, A and B), we observed that the anterior RFA region in eCS rats showed an increased vessel segment density (Fig. 6C) and cumulative vessel length (Fig. 6D) when compared to TBI control rats, whereas both TBI and eCS matrix–implanted animals demonstrated a marked reduction in these features compared to Sham (movies S1 to S4). We also observed that the posterior RFA showed a decreased density of vasculature in both TBI and eCS matrix–implanted animals. Notably, only three of five rats showed tissue presence in the RFAa ROI in TBI controls, whereas all animals in Sham and eCS matrix–implanted groups showed cellular and tissue presence. Tissue clearing and volumetric imaging revealed a larger propensity of tissue preservation in eCS matrix–implanted rats (movies S3 and S4) compared to TBI controls (fig. S13 and movie S2), which is consistent with lesion volume analysis obtained in Fig. 1. Using strong anion exchange (SAX) high-performance liquid chromatography (HPLC) analysis of CS sulfation profiles in brain tissue, we demonstrate that brain tissue isolated intralesionally from eCS matrix–implanted animals closely mimicked the CS sulfation profiles of Sham and perilesional tissue in TBI animals. These results also indicate a change in CS sulfation profile in brain tissue obtained from eCS matrix–implanted animals 4 weeks after TBI when compared to eCS matrix alone, suggesting integration and remodeling of the implanted eCS matrix (fig. S14 and table S1).

We found that the mean vessel diameters of vasculature in TBI controls and eCS matrix–implanted animals were not significantly different from those in Sham rats (Fig. 6E). However, consistent with the increased CBF observed in eCS matrix–implanted animals (Fig. 4, –20 weeks), the distribution of both vessel length density and diameter in RFAa was enhanced in eCS matrix–implanted rats when compared to Sham and TBI controls, as shown in Q-Q plots (fig. S15, A and B).

We found a significant correlation between $NeuN^+$ cells and vessel density (fig. S16A), and $NeuN^+$ cells and forelimb performance (fig. S16B). The correlation between vessel density and SRT performance also returns a strong Pearson's *R* value (fig. S16C), although not statistically significant. Together, these results indicate that eCS matrix implants promoted vascularization intralesionally (RFAa), which is strongly correlated with neuronal presence and forelimb performance in rats.

DISCUSSION

Parenchymal volume loss of brain tissue is highly correlated with the level of TBI severity in humans, with patients sustaining severe lesions experiencing significantly greater volume loss when compared to those who sustained mild TBIs (*59*). As a result, functional losses are inevitable and neuroplastic changes are limited, leaving patients with chronic and debilitating impairments (*1*). Studies on the intracortical implantation of brain-mimetic CS and hyaluronic acid GAG scaffolds after sTBI and stroke have demonstrated the ability to mediate complex structural and functional repair of brain tissue (*38*, *46*, *60*). The acute implantation of neurotrophic factor functionalized acellular eCS scaffolds that are compositionally similar to brain ECM could present a rational approach to mitigating the significant volume and functional losses encountered chronically after sTBI.

Using a materials design strategy that exploits the native functionality of CS, we demonstrate that neurotrophic factor–laden eCS matrix implants were neuroprotective and neurogenic and significantly enhanced the peri- and intralesional presence of newly formed blood vessels chronically after sTBI when compared to controls. The role of a global reduction of CBF and hypoperfusion in chronic dysfunction and poor prognosis after sTBI is well established (*53*–*57*). Our observations correlating enhanced vascular density to neuronal presence and reach-to-grasp function recovery suggest that eCS matrix implants orchestrate complex vascular repair that directly contributes to neuronal function and task-specific recovery chronically after sTBI. These effects are likely mediated by the enhanced presence and signaling of FGF2 and BDNF, which is potentiated by CS binding of these factors as demonstrated previously (*17*, *60*, *61*). We nonetheless interpret the implications of observed rCBF increase cautiously in the absence of comparative real-time cerebral oxygenation studies.

The compensatory reorganization of the motor cortex has been observed in perilesional circuitry and the contralateral hemisphere after TBI (*62*–*65*). In our studies, the volumetric quantification of Arc^+ neuronal populations following left-limb usage confirmed enhanced activity in both the perilesional and contralateral regions in TBI-only rats compared to Sham controls. eCS matrix–implanted rats showed a pattern of functional activity similar to TBI-only rats, with the added presence of intralesionally active neurons within the implant. Because BDNF expression is known to be regulated via autocrine signaling mechanisms (*66*) and could be contributing to enhanced neuroplasticity observed after brain injury (*62*, *63*, *67*), we speculate that enhanced transduction of neurotrophic factor signaling could be contributing to the observed enhancement in motor remapping (Fig. 3) and potentiation of FGF2 and BDNF expression in eCS matrix–implanted animals (*60*, *61*, *68*, *69*) when compared

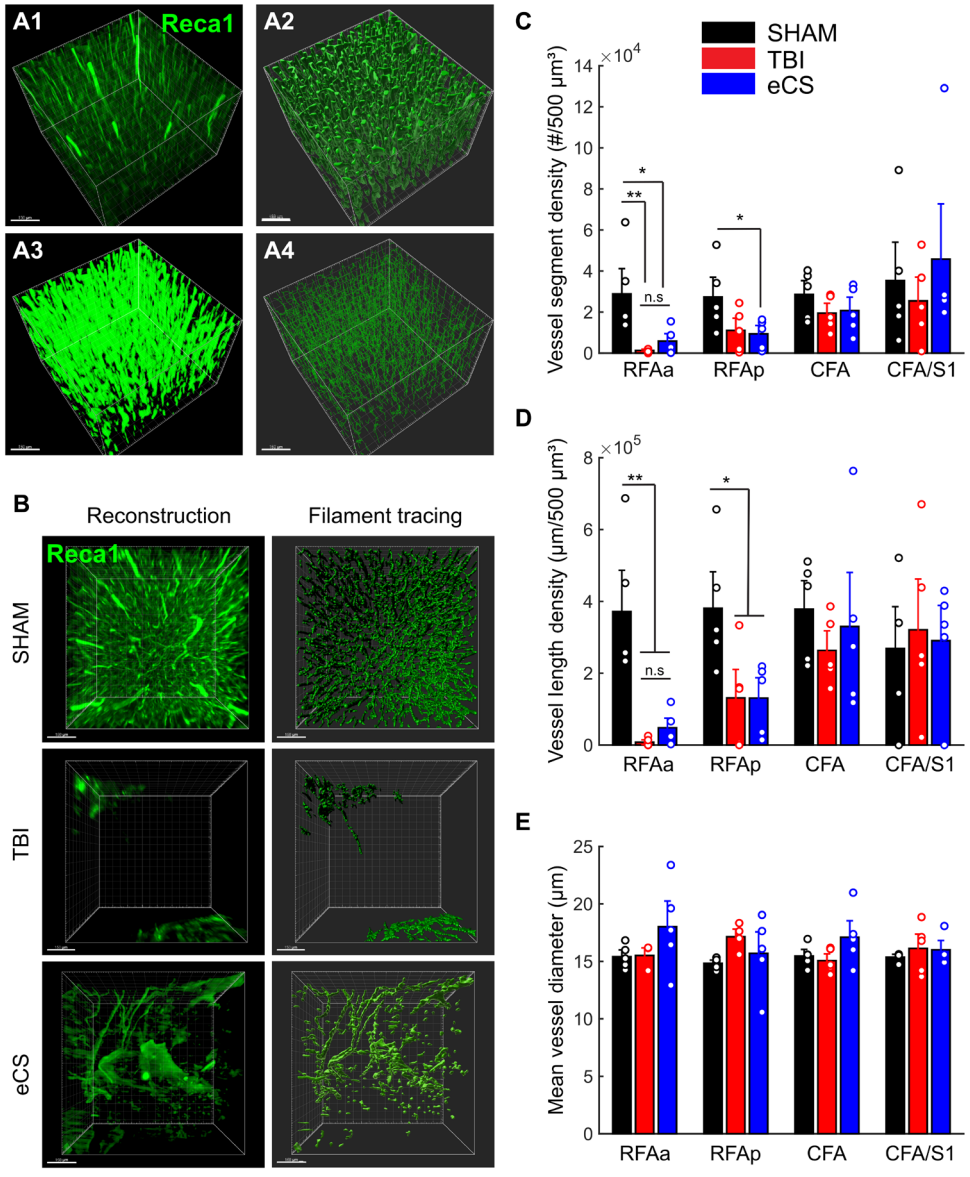

Fig. 6. eCS matrix implants promote changes in intra- and perilesional vascular architecture 8 weeks after sTBI. (**A**) Image processing step for vasculature tracing. Using Imaris software on volumetric images of iDisco$^+$ cleared brains, we first reconstructed volumetric images from Reca1$^+$ staining (green, A1) and performed surface mapping (A2), surface-based masking and Gaussian filtering (A3), and finally filament tracing (A4). Representative vascularization in eCS implanted region; original Reca1$^+$ images (left) and ROIs corresponding to vasculature tracing (right). (**B**) Representative images of Sham (top), TBI (middle), and eCS (bottom) rat brain tissue for the reconstructed original volume image (left) and vasculature tracing (right). (**C**) Quantification of blood vessel segment density per 500 µm^3 for Sham ($n = 15$), TBI ($n = 15$), and eCS ($n = 15$) groups in all four ROIs. (**D**) Quantification of blood vessel length density per micrometer/500 µm^3 for Sham ($n = 15$), TBI ($n = 15$), and eCS ($n = 15$) groups in all four ROIs. (**E**) Quantification of mean blood vessel diameter (volume: 500 µm^3) for Sham ($n = 15$), TBI ($n = 15$), and eCS ($n = 15$) groups in all four ROIs. Post hoc LSD Mann-Whitney *U* test, $^*P < 0.05$, $^{**}P < 0.01$, and $^{***}P < 0.001$. Bar graphs show means ± SEM. RFAa, RFA anterior; RFAp, RFA posterior/perilesional. Graphs show means ± SEM.

to TBI-only controls (Fig. 2). Our results also showed a close correspondence between Arc-dependent activation patterns and both electrophysiological response and recovery of forelimb-specific sensorimotor functions. This evidence suggests that intracortical eCS implants mediated the reorganization of neuronal circuitry, leading to chronic recovery of reach-to-grasp function after sTBI.

Subacute studies conducted 4 weeks after TBI have demonstrated the neuroprotective attributes of unmodified CS matrix implants (*46*). However, in light of evidence suggesting the poor prognostic implications of low BDNF levels acutely after sTBI (*70*), and function blocking studies demonstrating the direct role of BDNF in facilitating motor function recovery (*71*), strategies to enhance local signal transduction of neurotrophic factors as demonstrated in this study could offer significant therapeutic benefits. Despite the lack of eCS matrix presence 4 weeks after TBI as determined by SAX-HPLC analysis of brain tissue, our results imply that the complex cellular and vascular repair and functional recovery observed chronically in eCS matrix–implanted animals may have

been influenced by acutely implanted eCS matrices. Future investigations of the temporal effects of indwelling CS and eCS matrix implants on neurotrophic factor signaling will help better inform the design of more effective acellular eCS matrix implants for sTBI.

In summary, our results demonstrate that rationally designed, brain-mimetic, acellular eCS implants have native structure-function attributes required to mediate chronic tissue level repair and functional recovery after sTBI. This study opens up new avenues for the design and application of synthetic sulfated GAG constructs for brain tissue repair and informs future investigations of neuronal connectivity and electrophysiological responsiveness between the eCS matrix–implanted tissue and perilesional cortical columns.

MATERIALS AND METHODS

Animal procedures and preparation of eCS matrix

Animals

Sprague-Dawley rats were obtained for the 20-week (n = 33, 7 weeks old, males only; Harlan Laboratories) and 10-week experiments (n = 21, 3 weeks old, males only; Charles River Laboratories) and randomly assigned to each treatment: control craniotomy with no injury (Sham group: 20 weeks, n = 9; 10 weeks, n = 6), CCI (TBI group: 20 weeks, n = 9; 10 weeks, n = 6), and CCI implanted with eCS scaffolds (eCS group: 20 weeks, n = 15; 10 weeks, n = 9). A custom-designed controlled cortical impactor delivered the desired impact to the M1 motor cortex (20 weeks: CFA; AP (anterior-posterior): 0.5 mm; ML (medial-lateral): 0.5 mm, relatively to bregma; 10 weeks: RFA; AP: 3.0 mm; ML: 2.5 mm, relatively to bregma) of the eCS matrix–implanted animals and TBI-only controls.

All rats were singly housed with ad libitum access to food and water and following a reverse 12-hour light cycle (light OFF, 7:00 a.m. to 7:00 p.m.; light ON, 7:00 p.m. to 7:00 a.m.) in a room maintained at 70% humidity and 23°C. All procedures on animals were approved by the Institutional Animal Care and Use Committee, and protocols were performed in accordance with the *Guide for the Care and Use of Laboratory Animals* published by the National Institutes of Health (NIH).

Surgical procedures

Before CCI injury, each animal was anesthetized with 5% isoflurane and buprenorphine was injected subcutaneously (0.3 mg/ml, 0.05 ml/300 g; Henry Schein). Animals were placed on a stereotaxic frame attached to a temperature-controlled heating pad (37°C) with their scalp shaved and sanitized (70% EtOH and 3% povidone-iodine). Following a sagittal incision, the periosteum was cleaned using Etch Gel (Phosphoric Acid Etching, Henry Schein), and a craniotomy was performed using a 5-mm-diameter trephine bur fitted to an electronic drill. A 3-mm CCI tip was fitted onto the pneumatic piston and positioned in contact with the surface of the dura (fully extended position) and then retracted to adjust for an impact depth of 2 mm. A severe CCI injury was induced by programming the piston speed to 2.25 m/s and a dwell time of 250 ms, resulting in an initial 3-mm-diameter injury with a depth of 2 mm. Absorbable gelatin (Gelfoam, Pfizer) was applied to the injury site, and sterile cotton swabs were used to remove excess blood. The Gelfoam was then removed, and the injury site was covered completely with a layer of 1% sterile SeaKem (Lonza) agarose. Skin flaps were sutured together, closing the wound. Triple antibiotic cream was applied on the sutured skin.

Preparation and intralesional delivery of eCS matrix

Injured animals were randomly selected to receive intralesional injections of eCS matrix functionalized with the neurotrophic factors FGF2 (50 μg/ml; R&D Systems, 233FB025CF) and BDNF (50 μg/ml; R&D Systems, 248BDB010CF) 48 hours after sTBI. The eCS matrices were prepared using previously described methods (*17*, *46*) (22 μl: 8 μl of 10% methacrylated CSA-GAG; 7.58 μl of neurobasal media; 4 μl of 1% photocrosslinker Irgacure-2959; Sigma-Aldrich), loaded in a 50-μl Hamilton syringe (fitted blunted 21-gauge tight lock stainless steel needle). Because predominantly 4-O sulfated CS present in CS-A has been previously determined to bind with high affinity to FGF2 (K_D, 44 nM) and BDNF (K_D, 10 nM) (*17*), we preincubated half (11 μl) the injection volume containing methacrylated eCS matrix with BDNF (1.21 μl) and the other half with FGF2 (1.21 μl) to saturate binding sites and to affinity immobilize neurotrophic factors. The final 22 μl of injection volume containing eCS matrix–bound BDNF and FGF2 was loaded into a Hamilton syringe and photocrosslinked before intralesional injection. The 48-hour implantation time point was chosen as it was demonstrated to improve transplantation success (*72*) and facilitated optimal neuroprotective outcomes after TBI (*46*, *72*). Injections were performed after reopening the skin flaps following the above described procedure, removing the 1% agarose and positioning the syringe (angle of 32°, depth: 2 mm; speed: 2 μl/min for 10 min). Buprenorphine was administered (0.3 mg/ml, 0.05 ml/300 g; Henry Schein), and the skin was sutured back.

Behavioral assessment of functional recovery

Chronic functional recovery was assessed using longitudinal gross motor recovery assays including the beam-walk test (BW) (*73*), rotarod test (RTT) (*74*), and open field test (OFT) for time points corresponding to weeks 1, 2, 4, 6, 8, 10, 12, 14, 16, 18, and 20 after sTBI. Chronic recovery of forelimb-specific function was assessed using the SRT following preference and forced-side training at 1, 2, 4, 6, and 8 weeks after sTBI. All tasks were performed during the dark cycle in a red light lit room held at constant 70% humidity and 23°C.

Magnetic resonance imaging

MRI procedure

A 7-T Varian Magnex MRI scanner and a 35-mm dual-tuned surface coil were used to perform MRI of the brain to investigate the chronic (20 weeks) effects of sTBI. All animals were placed directly under isoflurane (1.5%) anesthesia on the holder of the animal-tube assembly, where a catheter was added to the tail of each rat intravenously with a line prefilled with 0.2 ml of heparin flush attached. The animal's head was securely positioned directly under the 20-mm dual-tuned surface coil, and the animal-tube assembly was placed inside the 210-mm horizontal bore of the small animal scanner. For each imaging sequence, eight coronal brain slices with 1-mm thickness and zero gap between slices were acquired using a field of 40 mm × 40 mm and a matrix size of 256 × 256. The following two imaging sequences were acquired for each animal: (i) T_2-weighted fast spin echo (T2WI): TR (time repetition) = 2.0 s, TE (time echo) = 32 ms, and 4 averages requiring an acquisition time of 4 min and 20 s and (ii) T_2*-weighted multigradient echo (MGEMS): TR = 600 ms, 8 echoes (TE = 10 to 45 ms in 5-ms increments), FA (flip angle) = 25°, and 4 averages requiring an acquisition time of 10 min and 14 s. Therefore, the total acquisition time for each animal was ~15 min.

Injury volume determination

As T2WI images revealed the largest areas of injury and inflammation, T2WI images were used to design an ROI library for each animal's injured cortex using ImageJ (NIH, MD) to manually segment the injured area.

Phase gradient mapping

The rate of flow in a blood vessel is inversely proportional to the change in phase between the vessel and the surrounding tissue (*75*). However, during MR acquisition, phase measurements are only recorded in the range of ±π, and any values that extend outside of this range get "wrapped," or forced into this range, making calculating the change in phase difficult in areas where wrapping occurs. Because the change in phase is proportional to the change in the phase gradient, phase gradient maps (PGMs) can be used to avoid this wrapping problem (*76*).

Changes in rCBF between groups were determined using the T^{2*}-weighted MGEMS data using the following procedure (*77*). PGMs were generated for each slice by calculating the magnitude of the phase gradients determined in the readout and phase encoding directions (*76*). From the PGMs, phase gradient differences between a vessel and the surrounding tissue were measured across all distinguishable vessels located within the cortex, subcortical and basal forebrain areas, and thalamus. The third echo (TE = 20 ms) was used for all measurements, as this echo produced the best contrast for distinguishing vessels within the PGMs. To account for systematic phase variations in the MRI acquisition across rats (differences in coil tuning, gradient shimming, etc.), measurements were normalized using the phase gradient difference measured across the third ventricle for each rat. Averages and SDs of all nPG differences were calculated for all vessels located on both the contralateral and ipsilateral side of the brain to the injury for each region and group.

Brain tissue preparation and immunohistochemistry

Tissue collection at 20-week time point

Twenty weeks after injury, animals were heavily sedated using ketamine (65 mg/kg) and transcardially perfused with 250 ml of 0.1 phosphate-buffered saline (PBS; pH 7.4). Brains were then extracted and cut in half (transversal cut), 7 mm from the apex of the frontal cortex, flash-frozen in liquid nitrogen, and stored at −80°C. Coronal sections were obtained using a Leica cryostat, starting from the center of the injury and moving caudally. A total of 48, 15-μm-thick sections were collected per animal and distributed evenly over 10 charged slides and 2 membrane slides (4 sections per slide). Two slides per animal were placed in 4% paraformaldehyde containing 4 M sucrose and stained with 0.1% cresyl violet solution to label Nissl bodies in neurons. The remaining eight charged slides were used for immunofluorescence assays, and the two membrane slides were used for quantitative reverse transcription polymerase chain reaction (qRT-PCR). For immunostaining, slides were dried and placed in 4% paraformaldehyde solution containing 4 M sucrose, assigned to one of the primary antibody groups, and incubated overnight at 4°C (Table 1). Slides were then incubated with blocking buffer consisting of 1:220 dilutions of appropriate secondary antibodies (Table 2), counterstained with cell nuclear stain (NucBlue, Life Technologies, NY), mounted with Fluoromount-G (Southern Biotech, AL), sealed with coverslips, and stored at −20°C until imaged.

Laser capture microdissection

LCM was performed on two membrane slides per animal as previously described (*78*). In brief, brain tissue sections were placed on a cold block, fixed for 2 min in ice-cold 75% ethanol solution, and then rinsed thrice with ice-cold nuclease-free PBS (pH 7.4, Life Technologies). Brain sections were stained in a 1:220 dilution of goat anti-rat IgG + 500 U of ribonuclease (RNase) inhibitor (Life Technologies). After 1-hour exposure, sections were rinsed three times with nuclease-free PBS and dehydrated sequentially with 75, 95, and 100% ethanol for 15 s each. Sections were placed on the ice block to dry for 5 min before LCM using a laser microdissection microscope (Leica).

Quantitative RT-PCR

Total RNA was extracted from LCM processed tissue using a PicoPure RNA Isolation kit (Thermo Fisher Scientific) and quantified using a NanoDrop analyzer (Thermo Fisher Scientific). Pooled total RNA (100 ng equivalent) (five slices per animal; seven rats) was used to synthesize complementary DNA (cDNA) using an RT First Strand kit (Qiagen). Prevalidated primers targeting rat *CXCR4*, *CXCL12*, *BDNF*, and *FGF2*, along with the housekeeping genes *HPRT1* and *GAPDH* (Qiagen), were used in qRT-PCR assays for 40 cycles in three steps: 95°C for 10 min, 40 cycles of 95°C for 15 s, and 60°C for 1 min. Melting curve analysis was conducted to validate amplification specificity. All assays were conducted in triplicate on a 7900 HT instrument (Applied Biosystems), and gene expression levels were normalized to endogenous gene controls plotted as relative units using the $\Delta\Delta C_t$ method. Gene expression was analyzed with an absolute fold difference greater than 2. Gene expression was normalized against the average expression of Sham controls.

Tissue collection and preparation for task- and stimulation-specific activation of immediate early genes—10 weeks

For the visualization of functional activity in the whole brain, we used antibody staining against the immediate early gene–encoded actin-regulated cytoskeleton-associated protein (Arc). Two groups of rats were used at 10 weeks after sTBI. The first cohort of rats performed a continuous 40 min of SRT (specific left forelimb activation with high repetition; n = 3 to 4 per group) before being immediately sacrificed for tissue collection. The second cohort of rats was used for intracortical recordings and perilesional electrophysiological response to the left paw stimulation (see the "Electrophysiological recordings" section; n = 3 to 4 per group) before being sacrificed for tissue collection. These two cohorts were used to map the volumetric activation of neuronal networks in relation to either volitional control of the left forelimb (SRT cohort) or the sensorimotor response to paw stimulation. All brains were collected after transcardial perfusion with 250 ml of 1X PBS containing 4% paraformaldehyde, and processed for iDisco$^+$ tissue clearing.

iDisco$^+$ tissue clearing and immunostaining

Following post-fixation, the frontal sections of the brains were treated for immunostaining and tissue clearing using the iDisco$^+$ method (*79*) with steps described briefly in Table 3.

Tissue imaging and quantification

Brain slices were imaged using either a Zeiss LSM7100 confocal microscope (Zen software; immunostained slices), epifluorescence Leica DM IRBE (Volocity software; cresyl/Nissl stain slices), or LaVision Ultra II Light Sheet microscope (iDisco$^+$ cleared brains).

Image quantification for immunostained slices was performed using MATLAB and custom scripts based on the image processing toolbox. For cresyl violet–stained slides, the ROI represented 10.494 mm^2, and four images were taken per animal per group (n = 7, 28 total images). ImageJ (NIH, MD) was used to calculate and analyze the total number of marked Nissl bodies. Images were

Table 1. Primary antibody panel for immunostaining.

Purpose	Antibody	Manufacturer	Catalog no.	Host	Dilution	Usage
Neuronal presence/ marker	NeuN	EMD Millipore	MAB377	Mouse	1:500	Slices
Neuronal presence/ marker	NeuN	EMD Millipore	ABN91	Chicken	1:500	iDisco$^+$
Neuronal proliferation	Doublecortin (DCX)	Abcam	ab18723	Rabbit	1:500	Slices
Myelination	Olig2	Abcam	ab109186	Rabbit	1:100	Slices
Neural progenitor	Sox-1	Abcam	ab87775	Rabbit	1:1000	Slices
	Ki67	Santa Cruz	sc-7846	Goat	1:500	Slices
Neuroinflammation	GFAP	DAKO	z0334	Rabbit	1:1000	Slices
	CD68	Bio-Rad	mca341R	Mouse	1:500	Slices
Growth factor presence	FGF2	Abcam	ab8880	Rabbit	1:200	Slices
Chondroitin sulfate GAG presence	CS56	Sigma-Aldrich	C8035	Mouse	1:200	Slices
Plasticity	Synapsin-1	Abcam	ab14692	Rabbit	1:500	Slices
Neuronal activation marker	Arc	Synaptic Systems	156 003	Rabbit	1:1000	Slices/iDisco$^+$
Vasculature	RECA	Bio-Rad	MCA970R	Mouse	1:500	Slices/iDisco$^+$
	Col IV	Abcam	Ab19808	Rabbit	1:500	Slices

Table 2. Secondary antibody panel.

Alexa Fluor	Host	Reactivity	Isotype	Catalog no.	Company
488	Goat	Mouse	IgG (H+L)	A11006	Life Technologies
488	Goat	Chicken	IgY (H+L)	A11039	Life Technologies
647	Goat	Rabbit	IgG (H+L)	A21244	Life Technologies
488	Donkey	Goat	IgG (H+L)	A11055	Life Technologies
594	Goat	Mouse	IgG (H+L)	A11005	Life Technologies

thresholded to signal peak (~200). Only elements of surface area in the range 50 to 500 pixels were counted, and any noncellular bodies outside this range were removed using the subtraction tool. For volumetric images, all image stacks were converted and processed using the software Imaris (Bitplane). Nuclear counts (NeuN$^+$ and Arc$^+$ staining) and colocalization were performed using spot detection and spot colocalization. Vascular density (Reca1$^+$) and orientation were performed using a batch sequence of (i) surface mapping, (ii) surface model-based masking, (iii) masked image Gaussian filter, and (iv) filament tracing (closed loop) for vasculature parameter extraction.

eCS quantification and characterization

GAG isolation. Brain tissue and eCS matrix samples were reconstituted in 2 ml of 0.1 M tris-HCl (pH 8.0) containing 2 mM $CaCl_2$ and 1% Triton X-100. The samples were homogenized, pronase (1.6 mg) was added to bring the whole concentration up to 0.8 mg/ml, and the tissue was digested with shaking at 50°C. After 24 hours, a second 1.6-mg aliquot of pronase was added and digestion continued for 24 hours. Lastly, the enzyme was inactivated by heating to 100°C for 15 min. The buffer was adjusted to 2 mM $MgCl_2$, benzonase (100 mU) was added, and the sample was incubated for 2 hours at 37°C. After inactivation of the enzyme (15 min, 100°C), any undigested material was removed by centrifugation for 1 hour at 4000*g*. The supernatant was applied to a DEAE-Sepharose column, washed with ~10 column volumes of loading buffer (pH ~8 tris buffer, 0.1 M NaCl). The sample was applied to the column, reapplied, and washed with loading buffer. The sample was then eluted in 3CVs of elution buffer (pH ~8 tris buffer, 2 M NaCl). Following lyophilization to dryness, the salt was removed with a commercial PD-10 column and then relyophilized.

GAG lyase digestion. All of the isolated GAG material was used for lyase digestions with chondroitinase ABC. Briefly, a solution (100-µl total volume) of each of the samples was treated with chondroitinase ABC and incubated over 16 hours (pH 8). The

Table 3. iDisco$^+$tissue clearing steps. For primary and secondary antibody concentration, please refer to Tables 1 and 2. RT, room temperature; DCM, dichloromethane; DBE, dibenzyl ether; DMSO, dimethyl sulfoxide; PBS, phosphate-buffered saline; PTx2, 0.05% Triton X-100 in 1× PBS; PTwh, 0.0.5% Tween 20, 0.5 ml of heparin (10 mg/ml) in 1× PBS.

Process	Condition	Reagent	Solvent
Initial wash	15 min 3× in each	PTx2 and PTwh	1× PBS
Serial dehydration	1 hour each	20/40/60/80/100% methanol	1× PBS
Defatting	Overnight	DCM (66%, v/v)	Methanol
Bleaching	Overnight	H_2O_2 (5%, v/v)	Methanol
Serial rehydration	1 hour each	20/40/60/80/100% PBS	Methanol
Permeabilization	4 days	Triton X-100, 20% DMSO	1× PBS
Blocking	2 days	Goat serum (6%, v/v) and DMSO (10%, v/v)	PTx2
Primary antibody incubation	7 days, 37°C, 100 rpm	Goat serum (3%, v/v) and DMSO (5%, v/v)	PTx2
Wash	Overnight		PTwh
Secondary antibody incubation	6 days, 37°C, 100 rpm	Goat serum (3%, v/v) and DMSO (5%, v/v)	PTx2
Final dehydration	1 hour each	20/40/60/80/100% methanol	DiH_2O
Defatting	3 hour, RT	DCM (66%, v/v)	Methanol
Defatting	Overnight	DCM 100%	DCM
Final defatting/clearing	30 min—hold indefinitely	100% DBE	DBE

enzyme was inactivated by heating to 100°C for 5 min. Samples were centrifuged at 14,000 rpm for 30 min before introduction to the HPLC.

SAX-HPLC analysis of sulfated CS disaccharides. SAX-HPLC was carried out on an Agilent system using a 4.6 mm × 250 mm Waters Spherisorb analytical column with 5-μm particle size at 25°C. Solvent A: 2.5 mM sodium phosphate, pH 3.5. Solvent B: 2.5 mM sodium phosphate, 1.2 M NaCl, pH 3.5. The gradient settings used in this analysis were chondroitin/dermatan sulfate with a flow rate of 1.0 ml/min and a 10-μl injection volume of each sample:

Time (min)	%A	%B
0	97	3
10	80	20
30	75	25
55	0	100
65	0	100

Detection was performed by post-column derivatization. Briefly, the eluent from the column was combined with a 1:1 mixture of 0.25 M NaOH and 1% 2-cyanoacetamide pumped at a flow rate of 0.5 ml/min from a binary HPLC pump. The eluent was heated to 130°C in a 10-m reaction coil, then cooled in a 50-cm cooling coil, and directed into the instrument's fluorescence detector (λex = 346 nm, λem = 410). Commercial standard disaccharides (Dextra Laboratories) were used for identification of each disaccharide based on elution time, as well as calibration.

Electrophysiological recordings

Perilesional electrophysiological recordings

At week 8, rats that received RFA-targeted lesion were induced and maintained under anesthesia using a ketamine/xylazine cocktail (100 mg/kg) and placed on a stereotaxic frame. Following sagittal scalp incision, a craniotomy was performed caudally to the injury (AP: 0 mm, ML: 2 to 4 mm, relatively to bregma), followed by durotomy to allow for the insertion of a 32-channel silicone probe (Neuronexus). The silicone probe was then inserted in the motor area (position1: CFA, AP: 0 mm, ML: 2.5 mm) or sensorimotor area (position2: S1, AP: 0 mm, ML: 3.5 mm) at a depth of 2 mm from the surface of the brain. All recordings were performed with a single-shank, 32-channel linear probe with 50-μm spacing between recording sites (177 mm^2) and a maximum span of 1.6 mm (A1x32-6 mm-50-177-CM32, 15-μm thickness, Gen4, lot #P994). The probe reference was used as main reference, and a screw positioned above the right cerebellum was used as ground.

Neural data were digitalized and recorded at 20 kHz (unit gain) using a multichannel systems W2100 acquisition module and a wireless headstage (HS32-EXT-0.5mA, 16 bit). For spike analysis, the broadband electrophysiological data were real-time band pass–filtered (300 to 5000 Hz) and a baseline precalculated threshold was used as trigger to save spike waveforms and spike event timestamps (threshold: five SDs). All recordings were performed for 5 min following a 10-min stabilization.

Paw electrical stimulation evoked neural activity

Paw electrical stimulation was performed from a separate HS32-EXT-0.5mA headstage to provide isolated stimulation. The stimulating electrode was a stainless steel needle inserted in the footpad of the rat paw. Paw stimulations were performed at a fixed-intensity (50 μA), biphasic electrical pulse (1-ms phase 1) optimized to minimize recording artefacts while eliciting triggered neural response. The paw

stimulation pulses were repeated 120 times at a frequency of 1 Hz. Each stimulation was monitored using a light-emitting diode (LED) output through a synchronized TTL port to the recording system.

Statistical analysis

All statistical analyses were performed using SigmaPlot (SyStat Software Inc., CA) or MATLAB statistical toolbox (MathWorks Inc.). For multiple group comparison (e.g., immunohistochemistry quantifications, volume, or area quantification), we used a one-way analysis of variance (ANOVA) followed by a multiple comparison least significant difference (LSD) due to the low number of group (three groups, Sham, TBI, and eCS). For group comparison on the nPG analysis (MRI), we used a three-way ANOVA followed by multiple comparison using the LSD approach. For behavior data, we performed two-way repeated-measures ANOVA using between-factor group (three level: Sham, TBI, and eCS) and within-factor time with a post hoc multiple comparison based on the LSD. When necessary (failure of normality of sample distribution), nonparametric tests such as Kruskal-Wallis and Mann-Whitney *U* rank sum test were used in place of one-way ANOVA and *t* tests. For distribution comparisons, the measure of effect size (MATLAB toolbox, dabest estimation statistics) (*80*) was used to avoid bias due to high sample number as well as quartile-quartile plot against Sham distribution. For all tests, $P < 0.05$ was considered significant.

SUPPLEMENTARY MATERIALS

Supplementary material for this article is available at http://advances.sciencemag.org/cgi/content/full/7/10/eabe0207/DC1

View/request a protocol for this paper from *Bio-protocol*.

REFERENCES AND NOTES

1. V. G. Coronado, L. C. McGuire, M. Faul, D. Sugerman, W. Pearson, The epidemiology and prevention of TBI. *Brain Injury Med.*, 45–56 (2012).
2. S. Pluchino, L. Zanotti, B. Rossi, E. Brambilla, L. Ottoboni, G. Salani, M. Martinello, A. Cattalini, A. Bergami, R. Furlan, G. Comi, G. Constantin, G. Martino, Neurosphere-derived multipotent precursors promote neuroprotection by an immunomodulatory mechanism. *Nature* **436**, 266–271 (2005).
3. E. W. Baker, H. A. Kinder, F. D. West, Neural stem cell therapy for stroke: A multimechanistic approach to restoring neurological function. *Brain Behav.* **9**, e01214 (2019).
4. A. Wennersten, X. Meijer, S. Holmin, L. Wahlberg, T. Mathiesen, Proliferation, migration, and differentiation of human neural stem/progenitor cells after transplantation into a rat model of traumatic brain injury. *J. Neurosurg.* **100**, 88–96 (2004).
5. G. P. Liao, M. T. Harting, R. A. Hetz, P. A. Walker, S. K. Shah, C. J. Corkins, T. G. Hughes, F. Jimenez, S. C. Kosmach, M. C. Day, K. J. Tsao, D. A. Lee, L. L. Worth, J. E. Baumgartner, C. S. Cox Jr., Autologous bone marrow mononuclear cells reduce therapeutic intensity for severe traumatic brain injury in children. *Pediatr. Crit. Care Med.* **16**, 245–255 (2015).
6. S. C. Berman, C. Galpoththawela, A. A. Gilad, J. W. Bulte, P. Walczak, Long-term MR cell tracking of neural stem cells grafted in immunocompetent versus immunodeficient mice reveals distinct differences in contrast between live and dead cells. *Magn. Reson. Med.* **65**, 564–574 (2011).
7. J. Y. Li, N. S. Christophersen, V. Hall, D. Soulet, P. Brundin, Critical issues of clinical human embryonic stem cell therapy for brain repair. *Trends Neurosci.* **31**, 146–153 (2008).
8. A. S. Lee, C. Tang, M. S. Rao, I. L. Weissman, J. C. Wu, Tumorigenicity as a clinical hurdle for pluripotent stem cell therapies. *Nat. Med.* **19**, 998–1004 (2013).
9. K. Akita, A. von Holst, Y. Furukawa, T. Mikami, K. Sugahara, A. Faissner, Expression of multiple chondroitin/dermatan sulfotransferases in the neurogenic regions of the embryonic and adult central nervous system implies that complex chondroitin sulfates have a role in neural stem cell maintenance. *Stem Cells* **26**, 798–809 (2008).
10. M. Ida, T. Shuo, K. Hirano, Y. Tokita, K. Nakanishi, F. Matsui, S. Aono, H. Fujita, Y. Fujiwara, T. Kaji, A. Oohira, Identification and functions of chondroitin sulfate in the milieu of neural stem cells. *J. Biol. Chem.* **281**, 5982–5991 (2006).
11. R. U. Margolis, R. K. Margolis, R. Santella, D. M. Atherton, The hyaluronidase of brain. *J. Neurochem.* **19**, 2325–2332 (1972).
12. E. Ruoslahti, Structure and biology of proteoglycans. *Annu. Rev. Cell Biol.* **4**, 229–255 (1988).
13. S. Sirko, K. Akita, A. Von Holst, A. Faissner, Structural and functional analysis of chondroitin sulfate proteoglycans in the neural stem cell niche. *Methods Enzymol.* **479**, 37–71 (2010).
14. S. Sirko, A. von Holst, A. Weber, A. Wizenmann, U. Theocharidis, M. Götz, A. Faissner, Chondroitin sulfates are required for fibroblast growth factor-2-dependent proliferation and maintenance in neural stem cells and for epidermal growth factor-dependent migration of their progeny. *Stem Cells* **28**, 775–787 (2010).
15. S. Sirko, A. von Holst, A. Wizenmann, M. Gotz, A. Faissner, Chondroitin sulfate glycosaminoglycans control proliferation, radial glia cell differentiation and neurogenesis in neural stem/progenitor cells. *Development* **134**, 2727–2738 (2007).
16. J. H. Seo, J. H. Yu, H. Suh, M. S. Kim, S. R. Cho, Fibroblast growth factor-2 induced by enriched environment enhances angiogenesis and motor function in chronic hypoxic-ischemic brain injury. *PLOS ONE* **8**, e74405 (2013).
17. L. Karumbaiah, S. F. Enam, A. C. Brown, T. Saxena, M. I. Betancur, T. H. Barker, R. V. Bellamkonda, Chondroitin sulfate glycosaminoglycan hydrogels create endogenous niches for neural stem cells. *Bioconjug. Chem.* **26**, 2336–2349 (2015).
18. S. S. Deepa, Y. Umehara, S. Higashiyama, N. Itoh, K. Sugahara, Specific molecular interactions of oversulfated chondroitin sulfate E with various heparin-binding growth factors. Implications as a physiological binding partner in the brain and other tissues. *J. Biol. Chem.* **277**, 43707–43716 (2002).
19. C. D. Nandini, K. Sugahara, Role of the sulfation pattern of chondroitin sulfate in its biological activities and in the binding of growth factors. *Adv. Pharmacol.* **53**, 253–279 (2006).
20. D. Carulli, T. Laabs, H. M. Geller, J. W. Fawcett, Chondroitin sulfate proteoglycans in neural development and regeneration. *Curr. Opin. Neurobiol.* **15**, 116–120 (2005).
21. A. Dityatev, M. Schachner, Extracellular matrix molecules and synaptic plasticity. *Nat. Rev. Neurosci.* **4**, 456–468 (2003).
22. R. Frischknecht, M. Heine, D. Perrais, C. I. Seidenbecher, D. Choquet, E. D. Gundelfinger, Brain extracellular matrix affects AMPA receptor lateral mobility and short-term synaptic plasticity. *Nat. Neurosci.* **12**, 897–904 (2009).
23. C. I. Gama, S. E. Tully, N. Sotogaku, P. M. Clark, M. Rawat, N. Vaidehi, W. A. Goddard III, A. Nishi, L. C. Hsieh-Wilson, Sulfation patterns of glycosaminoglycans encode molecular recognition and activity. *Nat. Chem. Biol.* **2**, 467–473 (2006).
24. M. E. Woodbury, T. Ikezu, Fibroblast growth factor-2 signaling in neurogenesis and neurodegeneration. *J. NeuroImmune Pharmacol.* **9**, 92–101 (2014).
25. M. M. Tang, W. J. Lin, J. T. Zhang, Y. W. Zhao, Y. C. Li, Exogenous FGF2 reverses depressive-like behaviors and restores the suppressed FGF2-ERK1/2 signaling and the impaired hippocampal neurogenesis induced by neuroinflammation. *Brain Behav. Immun.* **66**, 322–331 (2017).
26. A. G. Dayer, B. Jenny, M. O. Sauvain, G. Potter, P. Salmon, E. Zgraggen, M. Kanemitsu, E. Gascon, S. Sizonenko, D. Trono, J. Z. Kiss, Expression of FGF-2 in neural progenitor cells enhances their potential for cellular brain repair in the rodent cortex. *Brain* **130**, 2962–2976 (2007).
27. M. H. Monfils, I. Driscoll, H. Kamitakahara, B. Wilson, C. Flynn, G. C. Teskey, J. A. Kleim, B. Kolb, FGF-2-induced cell proliferation stimulates anatomical, neurophysiological and functional recovery from neonatal motor cortex injury. *Eur. J. Neurosci.* **24**, 739–749 (2006).
28. S. Yoshimura, T. Teramoto, M. J. Whalen, M. C. Irizarry, Y. Takagi, J. Qiu, J. Harada, C. Waeber, X. O. Breakefield, M. A. Moskowitz, FGF-2 regulates neurogenesis and degeneration in the dentate gyrus after traumatic brain injury in mice. *J. Clin. Invest.* **112**, 1202–1210 (2003).
29. C. Cunha, R. Brambilla, K. L. Thomas, A simple role for BDNF in learning and memory? *Front. Mol. Neurosci.* **3**, 1 (2010).
30. A. Chen, L. J. Xiong, Y. Tong, M. Mao, The neuroprotective roles of BDNF in hypoxic ischemic brain injury. *Biomed. Rep.* **1**, 167–176 (2013).
31. G. S. Griesbach, D. A. Hovda, R. Molteni, A. Wu, F. Gomez-Pinilla, Voluntary exercise following traumatic brain injury: Brain-derived neurotrophic factor upregulation and recovery of function. *Neuroscience* **125**, 129–139 (2004).
32. W. Xuan, T. Agrawal, L. Huang, G. K. Gupta, M. R. Hamblin, Low-level laser therapy for traumatic brain injury in mice increases brain derived neurotrophic factor (BDNF) and synaptogenesis. *J. Biophotonics* **8**, 502–511 (2015).
33. H. Chu, J. Gao, C. W. Chen, J. Huard, Y. Wang, Injectable fibroblast growth factor-2 coacervate for persistent angiogenesis. *Proc. Natl. Acad. Sci. U.S.A.* **108**, 13444–13449 (2011).
34. A. Y. Fouda, A. Alhusban, T. Ishrat, B. Pillai, W. Eldahshan, J. L. Waller, A. Ergul, S. C. Fagan, Brain-derived neurotrophic factor knockdown blocks the angiogenic and protective effects of angiotensin modulation after experimental stroke. *Mol. Neurobiol.* **54**, 661–670 (2017).
35. P. Kermani, B. Hempstead, BDNF Actions in the cardiovascular system: Roles in development, adulthood and response to injury. *Front. Physiol.* **10**, 455 (2019).
36. M. Modo, S. F. Badylak, A roadmap for promoting endogenous in situ tissue restoration using inductive bioscaffolds after acute brain injury. *Brain Res. Bull.* **150**, 136–149 (2019).

37. S. Mizumoto, D. Fongmoon, K. Sugahara, Interaction of chondroitin sulfate and dermatan sulfate from various biological sources with heparin-binding growth factors and cytokines. *Glycoconj. J.* **30**, 619–632 (2013).
38. L. R. Nih, S. Gojgini, S. T. Carmichael, T. Segura, Dual-function injectable angiogenic biomaterial for the repair of brain tissue following stroke. *Nat. Mater.* **17**, 642–651 (2018).
39. M. C. Tate, D. A. Shear, S. W. Hoffman, D. G. Stein, M. C. LaPlaca, Biocompatibility of methylcellulose-based constructs designed for intracerebral gelation following experimental traumatic brain injury. *Biomaterials* **22**, 1113–1123 (2001).
40. W. M. Tian, S. P. Hou, J. Ma, C. L. Zhang, Q. Y. Xu, I. S. Lee, H. D. Li, M. Spector, F. Z. Cui, Hyaluronic acid–poly-D-lysine-based three-dimensional hydrogel for traumatic brain injury. *Tissue Eng.* **11**, 513–525 (2005).
41. P. Hao, H. Duan, F. Hao, L. Chen, M. Sun, K. S. Fan, Y. E. Sun, D. Williams, Z. Yang, X. Li, Neural repair by NT3-chitosan via enhancement of endogenous neurogenesis after adult focal aspiration brain injury. *Biomaterials* **140**, 88–102 (2017).
42. C. Martínez-Ramos, U. Gómez-Pinedo, J. M. Soria, J. A. Barcia, M. M. Pradas, Neural tissue regeneration in experimental brain injury model with channeled scaffolds of acrylate copolymers. *Neurosci. Lett.* **598**, 96–101 (2015).
43. L. Zhou, J. Tu, G. Fang, L. Deng, X. Gao, K. Guo, J. Kong, J. Lv, W. Guan, C. Yang, Combining PLGA scaffold and MSCs for brain tissue engineering: A potential tool for treatment of brain injury. *Stem Cells Int.* **2018**, 1–8 (2018).
44. K.-F. Huang, W.-C. Hsu, W.-T. Chiu, J.-Y. Wang, Functional improvement and neurogenesis after collagen-GAG matrix implantation into surgical brain trauma. *Biomaterials* **33**, 2067–2075 (2012).
45. L. Zhang, F. Zhang, Z. Weng, B. N. Brown, H. Yan, X. M. Ma, P. S. Vosler, S. F. Badylak, C. E. Dixon, X. T. Cui, J. Chen, Effect of an inductive hydrogel composed of urinary bladder matrix upon functional recovery following traumatic brain injury. *Tissue Eng. Part A* **19**, 1909–1918 (2013).
46. M. I. Betancur, H. D. Mason, M. Alvarado-Velez, P. V. Holmes, R. V. Bellamkonda, L. Karumbaiah, Chondroitin sulfate glycosaminoglycan matrices promote neural stem cell maintenance and neuroprotection post-traumatic brain injury. *ACS Biomater Sci. Eng.* **3**, 420–430 (2017).
47. P. A. Walker, S. K. Shah, M. T. Harting, C. S. Cox Jr., Progenitor cell therapies for traumatic brain injury: Barriers and opportunities in translation. *Dis. Model. Mech.* **2**, 23–38 (2009).
48. L. R. Nih, S. T. Carmichael, T. Segura, Hydrogels for brain repair after stroke: An emerging treatment option. *Curr. Opin. Biotechnol.* **40**, 155–163 (2016).
49. R. Janz, T. C. Südhof, R. E. Hammer, V. Unni, S. A. Siegelbaum, V. Y. Bolshakov, Essential roles in synaptic plasticity for synaptogyrin I and synaptophysin I. *Neuron* **24**, 687–700 (1999).
50. A. Kumar, D. J. Loane, Neuroinflammation after traumatic brain injury: Opportunities for therapeutic intervention. *Brain Behav. Immun.* **26**, 1191–1201 (2012).
51. J. J. Moon, J. E. Saik, R. A. Poché, J. E. Leslie-Barbick, S. H. Lee, A. A. Smith, M. E. Dickinson, J. L. West, Biomimetic hydrogels with pro-angiogenic properties. *Biomaterials* **31**, 3840–3847 (2010).
52. G. Goldenberg, W. Oder, J. Spatt, I. Podreka, Cerebral correlates of disturbed executive function and memory in survivors of severe closed head injury: A SPECT study. *J. Neurol. Neurosurg. Psychiatry* **55**, 362–368 (1992).
53. M. Ichise, D. G. Chung, P. Wang, G. Wortzman, B. G. Gray, W. Franks, Technetium-99m-HMPAO SPECT, CT and MRI in the evaluation of patients with chronic traumatic brain injury: A correlation with neuropsychological performance. *J. Nucl. Med.* **35**, 217–226 (1994).
54. W. Oder, G. Goldenberg, J. Spatt, I. Podreka, H. Binder, L. Deecke, Behavioural and psychosocial sequelae of severe closed head injury and regional cerebral blood flow: A SPECT study. *J. Neurol. Neurosurg. Psychiatry* **55**, 475–480 (1992).
55. L. Prayer, D. Wimberger, W. Oder, J. Kramer, E. Schindler, I. Podreka, H. Imhof, Cranial MR imaging and cerebral 99mTc HM-PAO-SPECT in patients with subacute or chronic severe closed head injury and normal CT examinations. *Acta Radiol.* **34**, 593–599 (1993).
56. Y. Inoue, T. Shiozaki, O. Tasaki, T. Hayakata, H. Ikegawa, K. Yoshiya, T. Fujinaka, H. Tanaka, T. Shimazu, H. Sugimoto, Changes in cerebral blood flow from the acute to the chronic phase of severe head injury. *J. Neurotrauma* **22**, 1411–1418 (2005).
57. J. Kim, J. Whyte, S. Patel, B. Avants, E. Europa, J. Wang, J. Slattery, J. C. Gee, H. B. Coslett, J. A. Detre, Resting cerebral blood flow alterations in chronic traumatic brain injury: An arterial spin labeling perfusion FMRI study. *J. Neurotrauma* **27**, 1399–1411 (2010).
58. B. M. Ances, E. Zarahn, J. H. Greenberg, J. A. Detre, Coupling of neural activation to blood flow in the somatosensory cortex of rats is time-intensity separable, but not linear. *J. Cereb. Blood Flow Metab.* **20**, 921–930 (2000).
59. B. Levine, N. Kovacevic, E. I. Nica, G. Cheung, F. Gao, M. L. Schwartz, S. E. Black, The Toronto traumatic brain injury study: Injury severity and quantified MRI. *Neurology* **70**, 771–778 (2008).
60. M. R. M. Crary, K. Jesson, Z. Z. Wei, M. Logun, C. Lenear, S. Tan, X. Gu, M. Q. Jiang, L. Karumbaiah, S. P. Yu, L. Wei, Cortical transplantation of brain-mimetic glycosaminoglycan scaffolds and neural progenitor cells promotes vascular regeneration and functional recovery after ischemic stroke in mice. *Adv. Healthc. Mater.* **9**, e1900285 (2020).
61. P. Milev, H. Monnerie, S. Popp, R. K. Margolis, R. U. Margolis, The core protein of the chondroitin sulfate proteoglycan phosphacan is a high-affinity ligand of fibroblast growth factor-2 and potentiates its mitogenic activity. *J. Biol. Chem.* **273**, 21439–21442 (1998).
62. R. J. Nudo, Adaptive plasticity in motor cortex: Implications for rehabilitation after brain injury. *J. Rehabil. Med.* **2003**, 7–10 (2003).
63. R. J. Nudo, Mechanisms for recovery of motor function following cortical damage. *Curr. Opin. Neurobiol.* **16**, 638–644 (2006).
64. S. Y. Kim, J. E. Hsu, L. C. Husbands, J. A. Kleim, T. A. Jones, Coordinated plasticity of synapses and astrocytes underlies practice-driven functional vicariation in peri-infarct motor cortex. *J. Neurosci.* **38**, 93–107 (2018).
65. D. S. Ramanathan, L. Guo, T. Gulati, G. Davidson, A. K. Hishinuma, S. J. Won, R. T. Knight, E. F. Chang, R. A. Swanson, K. Ganguly, Low-frequency cortical activity is a neuromodulatory target that tracks recovery after stroke. *Nat. Med.* **24**, 1257–1267 (2018).
66. P. L. Cheng, A. H. Song, Y. H. Wong, S. Wang, X. Zhang, M. M. Poo, Self-amplifying autocrine actions of BDNF in axon development. *Proc. Natl. Acad. Sci. U.S.A.* **108**, 18430–18435 (2011).
67. D. Ramanathan, J. M. Conner, M. H. Tuszynski, A form of motor cortical plasticity that correlates with recovery of function after brain injury. *Proc. Natl. Acad. Sci. U.S.A.* **103**, 11370–11375 (2006).
68. D. Kurihara, T. Yamashita, Chondroitin sulfate proteoglycans down-regulate spine formation in cortical neurons by targeting tropomyosin-related kinase B (TrkB) protein. *J. Biol. Chem.* **287**, 13822–13828 (2012).
69. P. Yu, C. S. Pearson, H. M. Geller, Flexible roles for proteoglycan sulfation and receptor signaling. *Trends Neurosci.* **41**, 47–61 (2018).
70. F. K. Korley, R. Diaz-Arrastia, A. H. B. Wu, J. K. Yue, G. T. Manley, H. I. Sair, J. van Eyk, A. D. Everett; TRACK-TBI investigators including, D. O. Okonkwo, A. B. Valadka, W. A. Gordon, A. I. R. Maas, P. Mukherjee, E. L. Yuh, H. F. Lingsma, A. M. Puccio, D. M. Schnyer, Circulating brain-derived neurotrophic factor has diagnostic and prognostic value in traumatic brain injury. *J. Neurotrauma* **33**, 215–225 (2016).
71. M. Ploughman, V. Windle, C. L. MacLellan, N. White, J. J. Doré, D. Corbett, Brain-derived neurotrophic factor contributes to recovery of skilled reaching after focal ischemia in rats. *Stroke* **40**, 1490–1495 (2009).
72. D. A. Shear, C. C. Tate, M. C. Tate, D. R. Archer, M. C. LaPlaca, D. G. Stein, G. L. Dunbar, Stem cell survival and functional outcome after traumatic brain injury is dependent on transplant timing and location. *Restor. Neurol. Neurosci.* **29**, 215–225 (2011).
73. S. T. Fujimoto, L. Longhi, K. E. Saatman, V. Conte, N. Stocchetti, T. McIntosh, Motor and cognitive function evaluation following experimental traumatic brain injury. *Neurosci. Biobehav. Rev.* **28**, 365–378 (2004).
74. R. J. Hamm, B. R. Pike, D. M. O'Dell, B. G. Lyeth, L. W. Jenkins, The rotarod test: An evaluation of its effectiveness in assessing motor deficits following traumatic brain injury. *J. Neurotrauma* **11**, 187–196 (1994).
75. Y. Shen, Z. Kou, C. W. Kreipke, T. Petrov, J. Hu, E. M. Haacke, In vivo measurement of tissue damage, oxygen saturation changes and blood flow changes after experimental traumatic brain injury in rats using susceptibility weighted imaging. *Magn. Reson. Imaging* **25**, 219–227 (2007).
76. L. Wang, W. M. Potter, Q. Zhao, In vivo quantification of SPIO nanoparticles for cell labeling based on MR phase gradient images. *Contrast Media Mol. Imaging* **10**, 43–50 (2015).
77. G. Simchick, M. Betancur, L. Karumbaiah, Q. Zhao, Gauging the effectiveness of traumatic brain injury treatment using MR phase gradient mapping, in *Proceedings of the 24th Annual Meeting of ISMRM, Singapore, Singapore* (2016).
78. L. Karumbaiah, S. E. Norman, N. B. Rajan, S. Anand, T. Saxena, M. Betancur, R. Patkar, R. V. Bellamkonda, The upregulation of specific interleukin (IL) receptor antagonists and paradoxical enhancement of neuronal apoptosis due to electrode induced strain and brain micromotion. *Biomaterials* **33**, 5983–5996 (2012).
79. N. Renier, Z. Wu, D. J. Simon, J. Yang, P. Ariel, M. Tessier-Lavigne, iDISCO: A simple, rapid method to immunolabel large tissue samples for volume imaging. *Cell* **159**, 896–910 (2014).
80. J. Ho, T. Tumkaya, S. Aryal, H. Choi, A. Claridge-Chang, Moving beyond P values: Data analysis with estimation graphics. *Nat. Methods* **16**, 565–566 (2019).

Acknowledgments: We thank C.-J. Tsai (UGA Department of Genetics) for providing us access to the Leica laser capture microdissection microscope and S. Gandhi (UC Irvine) for insightful technical discussions. We also acknowledge technical assistance from M. Logun on preliminary surgeries and behavioral testing. **Funding:** This work was supported by an NIH (RO1NS099596) award to L.K. and partially supported by a Georgia Partners in Regenerative Medicine seed grant from the Regenerative Engineering and Medicine (REM) research center to R.V.B. and L.K. and an Alliance for Regenerative Rehabilitation Research and Training (AR^3T)

technology development grant to L.K. and C.-F.V.L. P.A. acknowledges NIH support (R24GM137782) for this work. **Author contributions:** C.-F.V.L., M.I.B., and L.K. designed experiments. C.-F.V.L., M.I.B., H.D.M., R.F., and M.K.S. performed all animal behavior experiments and surgeries. N.B. and L.K. performed LCM and qRT-PCR experiments. M.I.B. performed MRI imaging, and G.A.S. performed phase gradient analysis. C.-F.V.L., M.K.S., and A.A. performed the tissue clearing, volumetric imaging, and volumetric quantification. C.-F.V.L. and R.F. performed the electrophysiological recording. C.-F.V.L., M.K.S., R.F., N.B., and C.E.L. performed cryosectioning, staining, and imaging of all samples. C.-F.V.L., R.M., and N.B. performed immunohistochemistry-based quantification, behavior analysis, qRT-PCR analysis, and statistical analysis. S.A.A.-H. performed SAX-HPLC. S.A.A.-H. and P.A. analyzed SAX-HPLC data. C.-F.V.L., Q.Z., P.V.H., R.V.B., and L.K. wrote and edited the manuscript. **Competing interests:** The authors declare that they have no competing interests. **Data and materials availability:** All data needed to evaluate the conclusions in the paper are present in the paper and/or the Supplementary Materials. Data can be obtained on demand by contacting the corresponding author: Lohitash@uga.edu.

Submitted 27 July 2020
Accepted 21 January 2021
Published 5 March 2021
10.1126/sciadv.abe0207

Citation: C.-F. V. Latchoumane, M. I. Betancur, G. A. Simchick, M. K. Sun, R. Forghani, C. E. Lenear, A. Ahmed, R. Mohankumar, N. Balaji, H. D. Mason, S. A. Archer-Hartmann, P. Azadi, P. V. Holmes, Q. Zhao, R. V. Bellamkonda, L. Karumbaiah, Engineered glycomaterial implants orchestrate large-scale functional repair of brain tissue chronically after severe traumatic brain injury. *Sci. Adv.* **7**, eabe0207 (2021).